



Covering convection with thermal blankets: fluid–structure interactions in thermal convection

Jinzi Mac Huang^{1,2,†}

¹NYU-ECNU Institute of Physics and Institute of Mathematical Sciences, New York University Shanghai, Shanghai, China

²Applied Math Lab, Courant Institute, New York University, New York, USA

(Received 2 April 2024; revised 13 September 2024; accepted 17 December 2024)

The continental plates of Earth are known to drift over a geophysical time scale, and their interactions have led to some of the most spectacular geof ormations of our planet while also causing natural disasters such as earthquakes and volcanic activity. Understanding the dynamics of interacting continental plates is thus significant. In this work, we present a fluid mechanical investigation of the plate motion, interaction and dynamics. Through numerical experiments, we examine the coupling between a convective fluid and plates floating on top of it. With physical modelling, we show the coupling is both mechanical and thermal, leading to the thermal blanket effect: the floating plate is not only transported by the fluid flow beneath, it also prevents the heat from leaving the fluid, leading to a convective flow that further affects the plate motion. By adding several plates to such a coupled fluid–structure interaction, we also investigate how floating plates interact with each other, and show that under proper conditions, small plates can converge into a supercontinent.

Key words: Bénard convection, buoyancy-driven instability

1. Introduction

Fluid–structure interactions appear at many different scales on our planet, and perhaps the largest one is the continental plate tectonics (Plummer, McGeary & Carlson 2001). It is believed that this tectonic motion results from the thermal convection in Earth’s mantle (Kious & Tilling 1996), where the mantle materials behave like a fluid (Turcotte &

† Email address for correspondence: machuang@nyu.edu

Schubert 2002) that is heated from the core and cooled at the surface of Earth. Under gravity, this configuration of heating and cooling leads to thermal convection, whose circulation provides forcing to the continental plates through shearing. This is considered to be the simplest picture of plate tectonics; however, many details of the plate dynamics, like the periodic formation of supercontinents and the associated geological Wilson cycle (Burke 2011), require further investigation.

Laboratory experiments have proven to be an effective way of understanding the fluid–structure interaction behind the plate tectonics, with many successful studies that couple the thermally convective fluid to solid structures (Elder 1967; Howard, Malkus & Whitehead 1970; Whitehead 1972). Aimed at recovering the plate dynamics and understanding the associated fluid–structure interactions, a series of laboratory experiments was later conducted by Zhang & Libchaber (2000) and Zhong & Zhang (2005, 2007*a,b*). Shown in figure 1(*a*), this experiment employs water as the working fluid, and a heater beneath provides heating while the ventilation at the water–air interface provides cooling, resulting in Rayleigh–Bénard convection (Ahlers, Grossmann & Lohse 2009). A floating plate of size d is carefully placed on top of this convective domain of total length D . This moving plate with centre location x_p has only fluid force acting on it, unless it hits the wall on the left or the right. Large-scale circulations (Araujo, Grossmann & Lohse 2005; Brown & Ahlers 2007; Moore & Huang 2023) are observed to form in the convective fluid, as shown in figures 1(*a*) and 1(*c*). Depending on the location x_p , the plate can be either transported by the circulating fluid, or situated on top of a converging or diverging centre of the surface flow (this is the case shown in figure 1*a*). Interestingly, different plate motions are observed depending on its size: when the ratio between plate size d and tank width D is smaller than a critical number near 0.58, the plate oscillates between the two sidewalls as shown in figure 1(*b*); When this ratio is above the critical value, the plate is trapped at the centre of tank, as shown in figures 1(*b*) and 1(*c*).

Zhong, Zhang, and others investigated this transition of behaviours, and they discovered that the so-called thermal blanket effect is responsible here (Zhang & Libchaber 2000; Zhong & Zhang 2005, 2007*a,b*; Huang *et al.* 2018; Mao, Zhong & Zhang 2019; Mao 2021; Lowenstein 2024). In this theory, the floating plate serves as an insulator (like a blanket) on top of the convective fluid, hence the fluid beneath becomes warmer due to the lack of ventilation. The warm fluid then rises, creating a diverging surface flow as shown in figure 1(*a*) that can transport the plate. The coupling between the fluid and the floating plate therefore goes two ways: the plate modifies the flow temperature and leads to thermal convection; the formed convective flows transport the floating plate. Their interplay leads to non-trivial dynamics of the plate shown in figure 1(*b*), and the physically inspired Zhong–Zhang model (Zhong & Zhang 2005, 2007*a,b*) successfully captures the transition of dynamics. Recently, more careful investigations on the Zhong–Zhang model have led to new advancements in the stochastic (Huang *et al.* 2018) and dynamical (Lowenstein 2024) modelling of fluid–structure interactions.

While the laboratory experiments are conducted in a domain of fluid with finite size, numerical simulations can be conducted in a domain that resembles the mantle of Earth. The numerical work of Gurnis (1988) provides one of the first time-dependent simulations of continental drift, where the fluid domain is two-dimensional and periodic. After this, many more numerical works have investigated the details of continental drift (Zhong & Gurnis 1993; Lowman & Jarvis 1993, 1995, 1999; Lowman & Gable 1999; Zhong *et al.* 2000; Lowman, King & Gable 2001), engaging higher resolutions, more detailed modelling of fluid–structure interactions, and three-dimensional simulations of the interior of Earth. In recent years, the mobility of the continental plate has become a focus of

Covering convection with thermal blankets

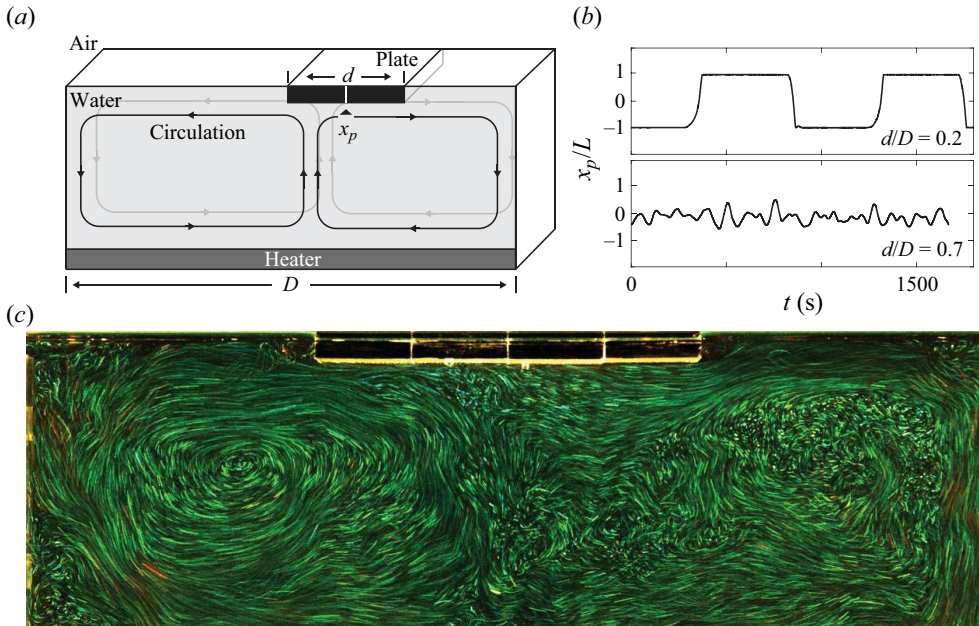


Figure 1. Rayleigh–Bénard convection coupled to a free-floating plate leads to different dynamics of plate motion. (a) Schematics of the interaction between Rayleigh–Bénard convection and the floating plate. The fluid is heated from below and has an open free surface; the floating plate on this free surface is transported by the fluid force exerted from below. (b) Different states of plate motion. A small plate with $d/D = 0.2$ oscillates between two sidewalls of the convection cell, while a big plate with $d/D = 0.7$ is trapped in the middle of the convection cell. Here, $L = (D - d)/2$ is the bound of plate centre x_p . (c) Flow visualization reveals two counter-rotating large-scale circulations when the plate is located at the centre of the convection cell. Image credit: Zhong & Zhang (2007b) and Huang *et al.* (2018).

numerical study, where persistent motion is observed for larger plates, while small plates tend to move sporadically (Gurnis 1988; Whitehead & Behn 2015; Mao *et al.* 2019; Mao 2021). In these works, the thermal blanket effect is once again recognized as an important factor causing the diverse plate dynamics.

This work is a continuation of an earlier investigation, Huang (2024), where the thermal and mechanical coupling between one floating plate and convective fluid is modelled through a simple stochastic model. This model shows that the covering ratio Cr , defined as the ratio of the plate area to the total surface area, is a direct measure of the thermal blanket effect. A critical covering ratio Cr^* is identified to distinguish the dynamics of the plate: for a small plate with $Cr \ll Cr^*$, the plate is passive to the flow field and exhibits little motion; for a plate with $Cr \gg Cr^*$, the strong thermal blanket effect leads to persistent plate translation. For plates with $Cr \approx Cr^*$, more complicated transitioning dynamics is observed.

In this work, we first introduce an efficient two-dimensional spectral solver that can accurately capture the motions and interactions of multiple floating plates on top of Rayleigh–Bénard convection. In a periodic domain shown in figure 2, this solver can handle the Navier–Stokes flows presented in laboratory experiments, with simple modifications available for the geophysical Stokes flows in the mantle. Moreover, multiple floating plates can be simulated as fast as a single-plate problem, as the floating plates are simply treated as an area with different boundary conditions. A specially tailored spectral solver handles the resulting inhomogeneous Robin conditions for both the temperature

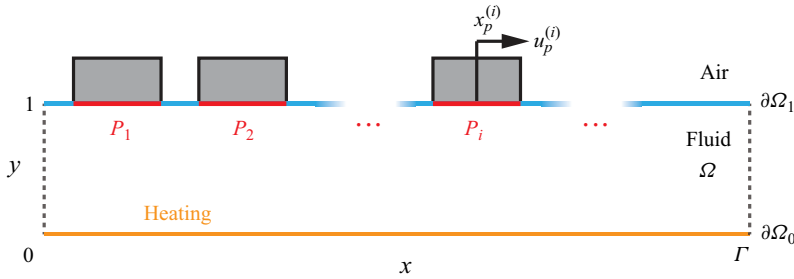


Figure 2. Schematics of the floating plate problem. The fluid domain Ω is heated from the bottom surface $\partial\Omega_0$, and has an open surface on top ($\partial\Omega_1$). Floating plates P_1, P_2, \dots cover part of this open surface, and shield the heat from leaving the fluid.

and the stream function, allowing for efficient time stepping and spectral accuracy. This enables us to systematically introduce one, two and many floating plates, and to show how the thermal blanket effect dictates their interactions with the convective flow beneath and each other. The covering ratio Cr is once again identified as a key factor affecting the plate dynamics and the stable formation of supercontinents.

This paper is arranged as follows. In § 2, we will mathematically formulate the Rayleigh–Bénard convection and its coupling to the plate motion. In § 3, a numerical scheme and its implementation for solving this free-boundary problem will be introduced. In § 4, numerical simulations of single, double and multiple plate dynamics will be included and discussed. Finally, we will discuss extensions and future works in § 5.

2. Mathematical formulation

2.1. Flow and temperature equations

We consider a dimensionless set of equations by rescaling the length scale by the cell height H , the time scale by the diffusion time H^2/κ (where κ is thermal diffusivity), and temperature by the temperature difference ΔT between the heater and the free surface. The x direction of the fluid domain is periodic with period $\Gamma = D/H$ (where D is the domain width), so the overall computational domain is $x \in (0, \Gamma), y \in (0, 1)$, as shown in figure 2. With the Boussinesq approximation, the resulting partial differential equations (PDEs) for flow speed $\mathbf{u} = (u, v)$, pressure p and temperature $\theta \in [0, 1]$ are

$$\frac{D\mathbf{u}}{Dt} = -\nabla p + Pr \nabla^2 \mathbf{u} + Ra Pr \theta, \tag{2.1}$$

$$\nabla \cdot \mathbf{u} = 0, \tag{2.2}$$

$$\frac{D\theta}{Dt} = \nabla^2 \theta. \tag{2.3}$$

Two dimensionless numbers appear during this non-dimensionalization: the Rayleigh number $Ra = \alpha g \Delta T H^3 / \nu \kappa$, and the Prandtl number $Pr = \nu / \kappa$, with ν, α and g denoting kinematic viscosity, thermal expansion coefficient of the fluid, and the acceleration due to gravity. We have further assumed that the physical properties of the fluid depend on temperature weakly, so Ra and Pr do not depend on θ .

As our simulation is two-dimensional, it is convenient to write the Navier–Stokes equation in a vorticity and stream function format (Peyret 2002):

$$\frac{D\omega}{Dt} = Pr \nabla^2 \omega + Pr Ra \frac{\partial \theta}{\partial x}, \quad (2.4)$$

$$-\nabla^2 \psi = \omega, \quad \mathbf{u} = \nabla_{\perp} \psi, \quad (2.5a,b)$$

$$\frac{D\theta}{Dt} = \nabla^2 \theta. \quad (2.6)$$

Instead of solving directly for \mathbf{u} and p , the z -component of vorticity $\omega = \mathbf{k} \cdot \nabla \times \mathbf{u}$ and the stream function defined by $\mathbf{u} = \nabla_{\perp} \psi = (\psi_y, -\psi_x)$ are solved first.

2.2. Boundary conditions

While (2.4)–(2.6) are standard for modelling Rayleigh–Bénard convection, the boundary conditions become complicated when floating plates are present. Shown in figure 2, the fluid domain Ω is bounded between the bottom heating wall $y = 0$ ($\partial\Omega_0$) and the top free surface $y = 1$ ($\partial\Omega_1$). The segments of top surface covered by the floating plates are labelled as P_1, P_2, \dots , whose centres are $x_p^{(1)}, x_p^{(2)}, \dots$.

The boundary conditions for the bottom heating wall are set straightforwardly as constant temperature and no-slip:

$$\theta = 1, \quad u = v = 0 \quad \text{at } y = 0. \quad (2.7)$$

For the vorticity–stream function format,

$$\theta = 1, \quad \psi = \psi_y = 0 \quad \text{at } y = 0. \quad (2.8)$$

The top condition consists of two types of regions: for the free surface (not covered by P_i), the temperature is low and the flow is shear-free; for the region covered by the plate P_i , the heat flux is zero and the flow shares the same velocity as the plate. The zero-flux condition originates from the ‘thermal blanket’ effect caused by the low heat conduction of solids. The boundary conditions at $y = 1$ can be summarized as

$$\theta = 0, \quad u_y = v = 0 \quad \text{for } y = 1 \text{ and } x \notin \bigcup P_i, \quad (2.9)$$

$$\theta_y = 0, \quad u = u_p^{(i)}, \quad v = 0 \quad \text{for } y = 1 \text{ and } x \in P_i. \quad (2.10)$$

Here, $u_p^{(i)} = \dot{x}_p^{(i)}$ is the velocity of i th plate P_i . For convenience, we can also write the top boundary conditions in a more compact way:

$$\begin{cases} (1 - a)\theta + a\theta_y = 0, \\ au + (1 - a)u_y = g \\ v = 0. \end{cases} \quad \text{at } y = 1, \quad (2.11)$$

For the vorticity–stream function format,

$$\begin{cases} (1 - a)\theta + a\theta_y = 0, \\ a\psi_y + (1 - a)\psi_{yy} = g \\ \psi = 0. \end{cases} \quad \text{at } y = 1, \quad (2.12)$$

Here, $a(x) = \sum_i \mathbb{1}_{x \in P_i}$, $g(x) = \sum_i u_p^{(i)} \mathbb{1}_{x \in P_i}$, and $\mathbb{1}_{x \in P_i}$ is the characteristic function such that

$$\mathbb{1}_{x \in P_i} = \begin{cases} 1 & \text{if } x \in P_i, \\ 0 & \text{otherwise.} \end{cases} \quad (2.13)$$

On plate P_i , two types of forces drive its motion: the fluid force $f^{(i)}$ due to the shear from convective flows, and the interacting force $f_l^{(i)}$ or $f_r^{(i)}$ when the left or right neighbouring plate (P_{i-1} or P_{i+1}) makes contact with plate P_i .

For the fluid force, we simply integrate the fluid shear stress:

$$f^{(i)} = -Pr \int_{P_i} u_y(x, 1, t) dx = -Pr \int_0^\Gamma u_y(x, 1, t) \mathbb{1}_{x \in P_i} dx. \quad (2.14)$$

The interaction forces $f_l^{(i)}$ and $f_r^{(i)}$ are modelled as a short-range interaction force to ensure a fully elastic collision between plates. The numerical implementations will be included in § 3.3.

Finally, we add all the forces together and evolve the plate location as

$$\dot{x}_p^{(i)} = u_p^{(i)}, \quad (2.15)$$

$$\dot{u}_p^{(i)} = a_p^{(i)} = m^{-1} \left[f_l^{(i)} + f_r^{(i)} - Pr \int_0^\Gamma u_y(x, 1, t) \mathbb{1}_{x \in P_i} dx \right]. \quad (2.16)$$

Here, $a_p^{(i)}$ is the acceleration of P_i , and m is the dimensionless mass of plate.

3. Numerical methods

3.1. Time stepping

We discretize time with the second order Adams–Bashforth backward differentiation method. At time step $t_n = n \Delta T$, (2.4)–(2.6) become

$$\nabla^2 \omega_n - \sigma_1 \omega_n = f_n, \quad (3.1)$$

$$\nabla^2 \theta_n - \sigma_2 \theta_n = h_n, \quad (3.2)$$

$$-\nabla^2 \psi_n = \omega_n, \quad (3.3)$$

where

$$\sigma_1 = \frac{3}{2 Pr \Delta t}, \quad \sigma_2 = \frac{3}{2 \Delta t}, \quad (3.4a,b)$$

$$f_n = Pr^{-1} \left[2(\mathbf{u} \cdot \nabla \omega)_{n-1} - (\mathbf{u} \cdot \nabla \omega)_{n-2} \right] - (2 Pr \Delta t)^{-1} (4\omega_{n-1} - \omega_{n-2}) - Ra \left(\frac{\partial \theta}{\partial x} \right)_n, \quad (3.5)$$

$$h_n = \left[2(\mathbf{u} \cdot \nabla \theta)_{n-1} - (\mathbf{u} \cdot \nabla \theta)_{n-2} \right] - (2 \Delta t)^{-1} (4\theta_{n-1} - \theta_{n-2}). \quad (3.6)$$

Equations (3.1)–(3.3) are Helmholtz equations that can be solved by standard numerical methods (Peyret 2002), and this implicit–explicit operator splitting scheme has been used in many numerical studies of thermal convection (Huang & Zhang 2022; Huang 2024).

However, modifications have to be made to accommodate the inhomogeneous Robin boundary conditions (2.12). We detail this modified Helmholtz solver in [Appendices A–C](#), and a flow chart of the numerical procedure can be found in [Appendix D](#).

In (3.5) and (3.6), nonlinear terms such as $\mathbf{u} \cdot \nabla \theta$ and $\mathbf{u} \cdot \nabla \omega$ are computed pseudo-spectrally, with a simple and efficient anti-aliasing filter (Hou & Li 2007). With given initial and boundary data, (3.2) can be solved first to obtain θ_n , which is inserted in f_n so (3.1) can be solved next. Finally, (3.3) is solved with the known ω_n . The spatial and temporal resolution of our study is also detailed in [Appendix D](#).

After solving for the flow and temperature fields, the acceleration $a_{p,n}^{(i)}$ of plate P_i can be computed via (2.16), and (2.15) and (2.16) are integrated with a second-order Adams–Bashforth method:

$$x_{p,n+1}^{(i)} = x_{p,n}^{(i)} + \frac{\Delta t}{2} \left[3u_{p,n}^{(i)} - u_{p,n-1}^{(i)} \right], \tag{3.7}$$

$$u_{p,n+1}^{(i)} = u_{p,n}^{(i)} + \frac{\Delta t}{2} \left[3a_{p,n}^{(i)} - a_{p,n-1}^{(i)} \right]. \tag{3.8}$$

3.2. Smooth boundary conditions

In principle, the introduced fluid and heat solver is able to manage the inhomogeneous Robin boundary condition (2.11) at $y = 1$. However, this boundary condition is not smooth, therefore limiting the accuracy of a numerical method with finite resolution. To overcome this, we aim to construct a smooth characteristic function $\hat{1}_{x \in P_i}$ so it is compactly supported and sufficiently smooth.

We first construct a smooth step function in one dimension, whose derivative $\phi_{l,m}(r)$ is in the family of Wendland functions that are shaped like a Gaussian (Chernih, Sloan & Womersley 2014):

$$\phi_{l,m}(r) = \begin{cases} \frac{1}{\Gamma(m) 2^{m-1}} \int_r^1 s(1-s)^l (s^2 - r^2)^{m-1} ds & \text{for } 0 \leq r \leq 1, \\ 0 & \text{for } r > 1. \end{cases} \tag{3.9}$$

The integer m controls the smoothness of the Wendland function, and $l = \lfloor m + n/2 \rfloor + 1$ for spatial dimension n . It can be shown that $\phi_{l,m} \in C^{2m}(\mathbb{R}^+)$, and it is compactly supported. Next, we take $m = 1$, $l = 2$ and construct a smooth step function $W_\epsilon(x)$ that transitions from 0 to 1 on $[-\epsilon, \epsilon]$:

$$W_\epsilon(x) = \frac{\int_{-\infty}^x \phi_{2,1}(|s|/\epsilon) ds}{\int_{-\infty}^{\infty} \phi_{2,1}(|s|/\epsilon) ds}. \tag{3.10}$$

This function is plotted in [figure 3\(a\)](#) with various ϵ , and it is easy to verify that $W_\epsilon(x) = 0$ when $x < -\epsilon$, and $W_\epsilon(x) = 1$ when $x > \epsilon$. As the transition length 2ϵ becomes smaller, W_ϵ becomes sharper, approximating a step function. Moreover, $W_\epsilon \in C^3(\mathbb{R})$ when $\epsilon > 0$ due to our choice of $m = 1$, achieving our goal of constructing a smooth step function.

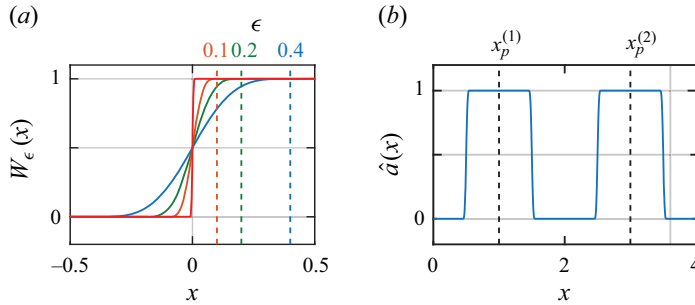


Figure 3. Smooth step and indicator functions. (a) Smooth step function W_ϵ that has transition interval $[-\epsilon, \epsilon]$. Four values of $\epsilon = 0.01, 0.1, 0.2, 0.4$ are plotted. (b) Smooth indicator function \hat{a} for locating the region of solid plates. The parameters plotted are $x_p^{(1)} = 1, x_p^{(2)} = 3, d = 1$ and $\epsilon = 0.05$.

We can further evaluate $W_\epsilon(x)$ as

$$W_\epsilon(x) = \begin{cases} 0 & \text{if } x < -\epsilon, \\ -\frac{3}{4} \left(\frac{x}{\epsilon}\right)^5 + \frac{5}{2} \left(\frac{x}{\epsilon}\right)^4 \operatorname{sgn}(x) - \frac{5}{2} \left(\frac{x}{\epsilon}\right)^3 + \frac{5}{4} \frac{x}{\epsilon} + \frac{1}{2} & \text{if } x \in [-\epsilon, \epsilon], \\ 1 & \text{if } x > \epsilon. \end{cases} \quad (3.11)$$

We next construct a smooth characteristic function $\hat{\mathbb{1}}_{x \in P}$ for a plate P centred at x_p with length d :

$$\hat{\mathbb{1}}_{x \in P_i} = W_\epsilon \left(x - \left(x_p - \frac{d}{2} \right) \right) W_\epsilon \left(\left(x_p + \frac{d}{2} \right) - x \right). \quad (3.12)$$

In our numerical examples, we take $\epsilon = 0.05d$ to ensure smoothness. Finally, we can write the Robin boundary conditions in the form

$$\begin{cases} (1 - \hat{a})\theta + \hat{a}\theta_y = 0, \\ \hat{a}u + (1 - \hat{a})u_y = \hat{g} \quad \text{at } y = 1, \\ v = 0, \end{cases} \quad (3.13)$$

where

$$\hat{a}(x) = \sum_i \hat{\mathbb{1}}_{x \in P_i}, \quad \hat{g}(x) = \sum_i u_p^{(i)} \hat{\mathbb{1}}_{x \in P_i}. \quad (3.14a,b)$$

Noticing that $W_\epsilon(0) = 0.5$, it can be verified easily that $\hat{a}(x) \in [0, 1]$ as long as $|x_p^{(i)} - x_p^{(j)}| \geq d$ for $i \neq j$. The function $\hat{a}(x)$ for two plates centred at $x_p^{(1)} = 1, x_p^{(2)} = 3$ with plate length $d = 1$ is shown in [figure 3\(b\)](#).

3.3. Dynamics of the moving plate

There are two types of forcing on each plate. One is the fluid force due to shear stress, and the other is the interaction force when two plates make contact.

For the fluid force, we simply integrate the shear stress by replacing the characteristic function with its smooth version:

$$f^{(i)} = -Pr \int_0^\Gamma u_y(x, 1, t) \hat{1}_{x \in P_i} dx = -Pr \Gamma \langle u_y \hat{1}_{x \in P_i} \rangle. \quad (3.15)$$

As we are using an equally spaced periodic grid in x , the integration can be replaced with a numerical average of all grid values of the integrand, so $\int_0^\Gamma f(x) dx \approx \Gamma \langle f \rangle = (\Gamma/L) \sum_{k=1}^L f_k$, which is spectrally accurate (Trefethen 2000).

When solid plates make contact, a contact force between them keeps the plates separated. Inspired by the experiments of Zhong & Zhang (2005, 2007a,b), we set the collision between neighbouring plates to be fully elastic, which means that their total momentum and kinetic energy are preserved after each collision. Numerically, we approximate the contact force by a function that is both short-ranged and smooth, so the force is zero when the plates are far away, but increases rapidly as they get close.

For plate number i , there are two forces for contact from the left neighbour and from the right neighbour:

$$f_l^{(i)} = f_{max} W_\delta \left(d - |x_p^{(i)} - x_p^{(i-1)}| \right), \quad (3.16)$$

$$f_r^{(i)} = -f_{max} W_\delta \left(d - |x_p^{(i+1)} - x_p^{(i)}| \right). \quad (3.17)$$

Here, the parameter δ models an ‘interaction length’, and f_{max} is the maximum interacting force between two plates. With the typical simulation parameters and no fluid forcing, we have verified that this choice of interacting force indeed conserves total momentum and results in a coefficient of restitution $e > 0.99$. At each simulation, δ and f_{max} are chosen according to the spatial and temporal resolution, so the ordinary differential equation (ODE) and PDE solvers can sufficiently resolve the plate motion and the associated boundary conditions.

4. Results

4.1. One-plate dynamics

In this subsection, we review the dynamics of a single plate motion. To simplify our study, the Rayleigh number is fixed at $Ra = 10^6$, the Prandtl number is $Pr = 7.9$, and the aspect ratio is $\Gamma = 4$. These parameters are similar to those in a previous numerical study (Huang 2024). For the plate, we set the mass as $m = 4d$, so plates with various lengths d have the same density. For the numerical solver, there are 512 Fourier modes in the x direction, and 129 Chebyshev nodes in the y direction, and the time step size is $\Delta t = 10^{-6}$. These parameters yield accurate, stable and resolved numerical solutions.

To measure the size of the plate, we define the covering ratio $Cr = d/\Gamma$. Depending on the size of the plate, or Cr , the dynamics of the plate motion can be very different. Figure 4 and supplementary movie 1 (available at <https://doi.org/10.1017/jfm.2024.1231>) show the dynamics of a small plate with $Cr = 0.1$, and its motion is a continuous random walk shown in figure 4(c). However in figure 5 and supplementary movie 2, a larger plate with $Cr = 0.6$ shows completely different dynamics: it translates unidirectionally as shown in figure 5(c).

In Huang (2024), the two dynamics are analysed in detail, and we summarize the key interplay between the plate and the fluid below.

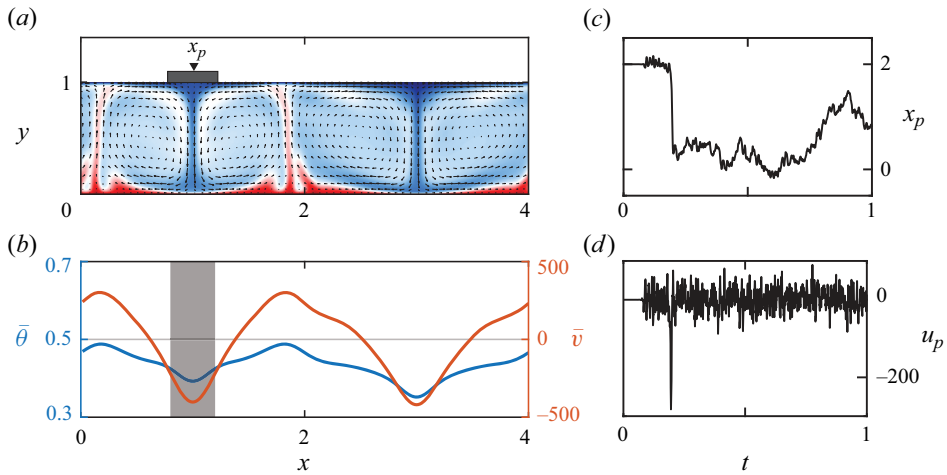


Figure 4. Motion of a small plate ($Cr = 0.1$) is random and bidirectional. (a) A snapshot of flow and temperature fields beneath a plate. The small plate is trapped at a cool converging centre. (b) Vertically averaged temperature $\bar{\theta}$ and vertical velocity \bar{v} at the same moment as in (a). The shaded region indicates the location of the plate. At the converging centre, the averaged temperature is low and the flow moves downwards. (c,d) The displacement x_p and velocity u_p of the plate show behaviour of a random walk with jumps.

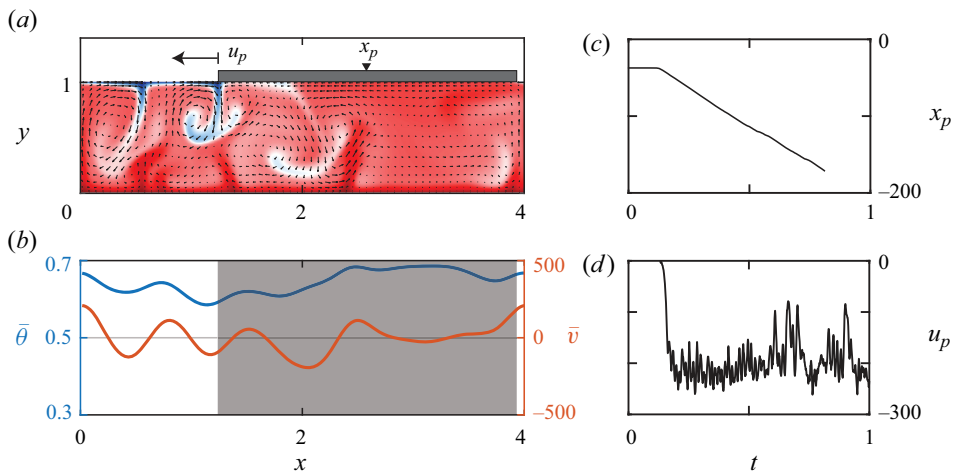


Figure 5. Motion of a large plate ($Cr = 0.6$) is unidirectional. (a,b) Flow and temperature fields beneath the plate. (c,d) The displacement x_p and velocity u_p of the moving plate, which shows unidirectional motion with non-zero mean velocity.

In figure 4, the small plate tends to be attracted by the converging centre of the fluid – the location where the fluid sinks. This converging centre can be seen clearly in figures 4(a) and 4(b), located at the minimum of both the vertically averaged temperature $\bar{\theta}(x, t) = \int_0^1 \theta(x, y, t) dy$ and the averaged vertical flow speed $\bar{v}(x, t) = \int_0^1 v(x, y, t) dy$. This means that the plate velocity $u_p = \dot{x}_p$ in figure 4(d) matches the translational velocity of the flow converging centre, which has a zero mean but is subject to noise due to random fluid forcing. In this case, the plate motion is passive and completely driven by the flow structure, and the converging centre of the surface flow serves as a stable equilibrium location for the plate.

Covering convection with thermal blankets

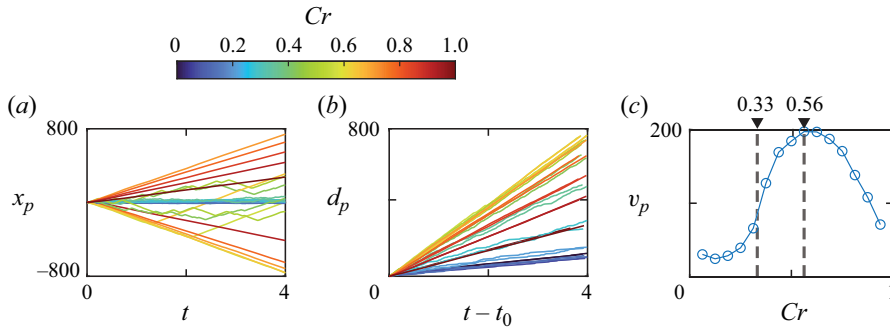


Figure 6. Plate displacement and velocity for different covering ratios Cr . (a) Sample trajectories of the plate location, where small plates are more affected by noise, and large plates have more persistent unidirectional motion. (b) Total travel of the plate reveals its speed; a maximum speed of travel can be seen at approximately $Cr = 0.6$. (c) Average travel speed has a maximum at $Cr = 0.56$, and unidirectional motions start to appear for plates larger than $Cr = 0.33$.

For a larger plate with $Cr = 0.6$, figure 5 and supplementary movie 2 show that the plate motion becomes unidirectional. Increasing plate size clearly changes the flow and temperature distribution in the fluid, as the bulk fluid temperature in figures 5(a,b) is visibly higher than that in figures 4(a,b). This is a clear sign of the thermal blanket effect, as the bigger plate shields the heat from escaping, and the effective cooling area at $y = 1$ is smaller. In this case, the plate is no longer passive, but creates a thermal blanket that warms the fluid beneath it. Unlike the situation of small plates, a large plate sitting on top of a converging centre cannot be stable in the long term, as eventually the temperature beneath the plate will become high enough to turn this converging centre into a divergent one. Shown in figure 5(b), the average temperature $\bar{\theta}$ is indeed higher below the plate, and the plate sits between the converging and diverging centres. This causes the unidirectional motion of the plate, and as the plate keeps affecting the temperature distribution beneath it, the temperature and flow fields move with the plate as shown in supplementary movie 2. The plate displacement x_p and velocity u_p are shown in figures 5(c) and 5(d), where u_p has a non-zero mean and is subject to random forcing from the fluid.

The motions of plates with various Cr are shown in figure 6. The displacement in figure 6(a) clearly shows that the small plate has a random motion whose net displacement grows slowly in time. As Cr increases, the plate starts to have more persistent unidirectional motions; however, the random fluid forcing can easily reverse the travel direction of the plate, leading to reversals of direction in figure 6(a). Further increasing Cr , the unidirectional motion becomes more persistent; however, the velocity (slope of x_p) decreases. Defining the total travel of a plate as $d_p(t) = \int_0^t |u_p(t')| dt'$, figure 6(b) shows a peak of the plate travelling speed at approximately $Cr = 0.6$. To further verify this, we define the average plate speed as $v_p = \lim_{t \rightarrow \infty} d_p(t)/t$ in figure 6(c), and a maximum indeed appears at $Cr = 0.6$.

As the thermal blanket effect strengthens, there is an apparent transition of the plate dynamics. Figure 7 shows the time series (lower images) and histogram (upper images) of u_p at various Cr . For small Cr , the histogram of plate velocity resembles a Gaussian distribution, whose zero mean suggests that the net plate displacement would be small. Increasing Cr beyond 0.3, the plate dynamics starts to transition as figure 7(c) shows that the variance of u_p increases. At $Cr = 0.4375$ (figure 7d), the two translational states

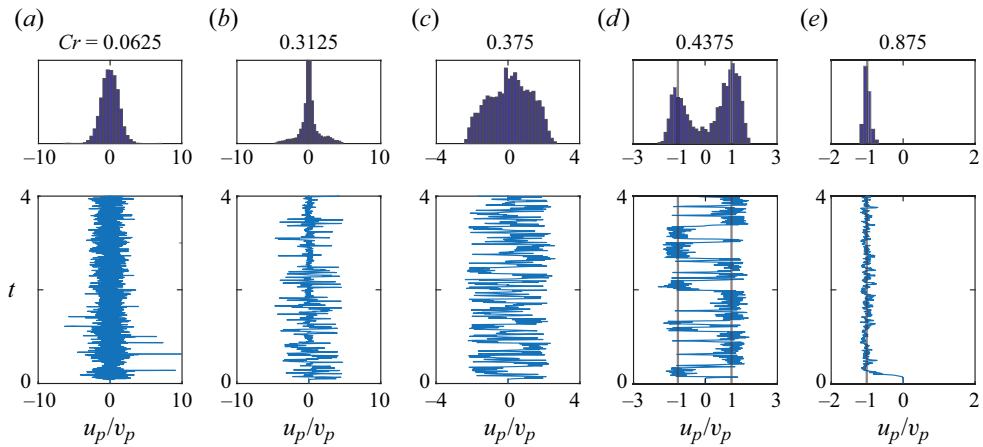


Figure 7. Time series (lower images) and histogram (upper images) of the plate velocity u_p at various Cr . The plate velocity is normalized by its average travel speed v_p , so $u_p \approx \pm v_p$ suggests a unidirectional translation. (a–e) Covering ratios 0.0625, 0.3125, 0.375, 0.4375, 0.875, respectively. The plate motion has a transition from the passive state in (a,b) to the translating state in (d,e), and the translation is also more persistent for large Cr in (e).

with $u_p = \pm v_p$ emerge, where u_p switches between the two directions due to the noise of fluid forcing. At even higher Cr (figure 7e), the unidirectional motion is persistent and the reversal becomes rare. The observation here matches the stochastic theory developed in Huang (2024), which consists of a simple model that recovers the mechanical and thermal interplay between the plate and the fluid. This stochastic model predicts that there is only a passive state (no net plate motion) for $Cr < Cr^*$, where the critical covering ratio is $Cr^* = 1/3$ for $\Gamma = 4$, and the translational states can exist only for plates with $Cr > Cr^*$, indeed matching figure 7.

Finally, we investigate how the bulk properties of the flow respond to the moving plate. In figure 8, we show the Nusselt number $Nu = -[\Gamma(t_2 - t_1)]^{-1} \int_{t_1}^{t_2} dt \int_0^\Gamma \theta_y(x, 0, t) dx$ and the Reynolds number $Re = (t_2 - t_1)^{-1} \int_{t_1}^{t_2} (\max_{(x,y)} |\mathbf{u}(x, y, t)|) dt$, where $t_2 - t_1$ is the interval for long-time average. The two groups of measurements are for a plate that is free to move by the flow (free), and for a plate that is fixed at a certain location (immobile). By setting the plate free, the Nusselt number changes slightly in figure 8(a), while the Reynolds number decreases significantly in figure 8(b). We also note that at the critical Cr^* , the flow speed reaches a maximum for the immobile plate shown in figure 8(b). Moreover, the Nusselt number approaches its maximum at approximately $Cr = 0.6$, where the plate translates the fastest, as shown in figure 6(c). While we do not have a clear theory to explain the observations in figure 8, we believe that the free plate motion certainly modifies the flow and thermal structure of Rayleigh–Bénard convection. For example, the fluid shearing drives the plate motion, thus part of the fluid kinetic energy must be converted to the plate kinetic energy. This may explain why a significant decrease of Re is shown in figure 8(b).

4.2. Two-plate interactions

Adding multiple plates to the convective surface brings interactions between plates and leads to more diverse dynamics. In our numerical simulation, adding a second plate can

Covering convection with thermal blankets

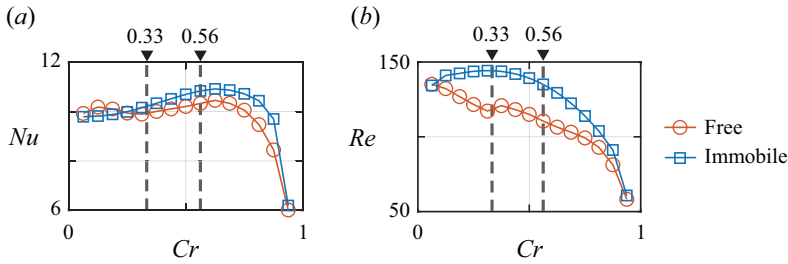


Figure 8. Nusselt and Reynolds numbers for the convecting flow. (a) The Nusselt number is a measure of the vertical heat passing through the flow. (b) The Reynolds number as a measure of flow speed. The free data are for the plate moving freely with the flow, and the immobile data are for the plate that is fixed.

be achieved easily through the indicator function method outlined in §§ 2 and 3. In the following numerical experiments, we set $Ra = 10^6$, $Pr = 7.9$, $\Gamma = 4$, $m = 4d$, as we did for the single-plate case. We additionally set the maximum interaction force $f_{max} = 10^6$ and an interaction range $\delta = \epsilon$ that matches the size of the smoothing region of the indicator function in § 3.2. These two parameters define the force of interaction between the two plates through (3.16) and (3.17), and such interaction conserves both the kinetic energy and momentum of the plates.

The dynamics of a pair of small plates (figure 9) and a pair of large plates (figure 10) are quite different. In figure 9 and supplementary movie 3, two small plates with individual covering ratios $Cr_p = 0.1$ are released on the convective surface. The two plates tend to stay together, generating a ‘supercontinent’ as shown in figure 9(a). Further analysing the flow temperature and surface flow rate in figure 9(b), we see they are in fact attracted by a converging centre of the surface flow, and the surface flow pushes them into each other. The trajectories $x_p^{(1)}$ and $x_p^{(2)}$ of the plates are shown in figure 9(c), and the normalized plate distance $d_{12} = [x_p^{(2)} - x_p^{(1)}] / \Gamma$ is plotted in figure 9(d). We see clearly that the two plates prefer to stay in contact, as the normalized distance stays near Cr_p or $1 - Cr_p$ in figure 9(d).

The combined covering ratio of these two plates is $Cr = 2Cr_p = 0.2$, which is less than the critical covering ratio $Cr^* = 1/3$ that we identified earlier. Therefore, the thermal blanket effect generated by this supercontinent is not strong enough to heat up the fluid beneath, and the surface flow stays converging and pushing the two plates together. Thus a supercontinent with combined $Cr < Cr^*$ is stable in its formation and exhibits a passive motion.

Figure 10 and supplementary movie 4 show the dynamics of two plates with $Cr = 2Cr_p = 0.6$. In this case, the fluid beneath the supercontinent is warmed up due to the thermal blanket effect, and generates an upwelling flow. The resulting diverging surface flow separates the two plates, leading to an unstable supercontinent formation. Figures 10(c) and 10(d) show the plate trajectories and the normalized plate distance, and the two plates are seen to stay separated in figure 10(d) as their normalized distance is between Cr_p and $1 - Cr_p$, and the contact state is only transient.

In figure 10, although the covering ratio for each plate satisfies $Cr_p < Cr^*$, their combined ratio is $Cr = 2Cr_p > Cr^*$. The supercontinent, once formed, will become unstable as the warm fluid beneath creates a diverging surface flow that pulls the two plates apart.

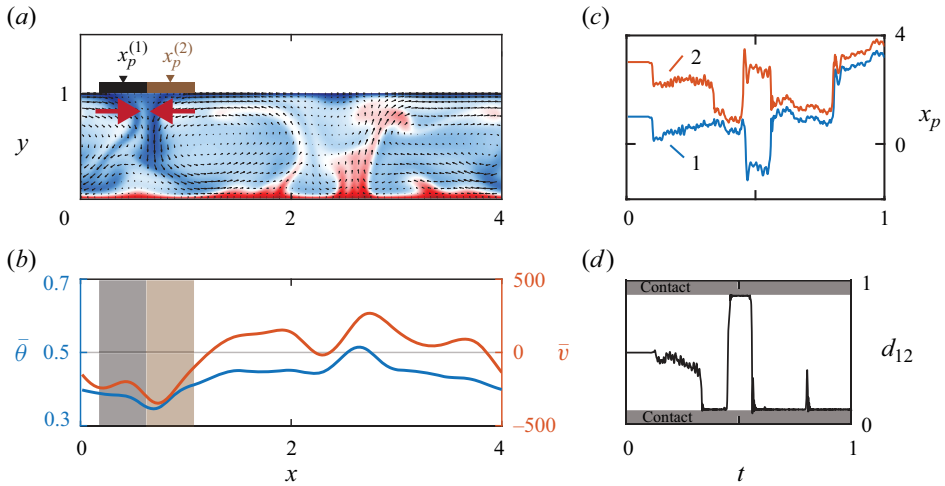


Figure 9. Dynamics of two small plates ($Cr_p = 0.1$ each) forming a supercontinent of $Cr = 0.2$. (a) Flow and temperature distribution beneath the supercontinent. The surface flow is converging, and the formation of the supercontinent is stable. (b) Vertically averaged temperature $\bar{\theta}$ and vertical velocity \bar{v} at the same moment as in (a), with the region of the two plates shaded. (c) The displacement of plates $x_p^{(1)}$ and $x_p^{(2)}$. (d) The normalized plate distance $d_{12} = [x_p^{(2)} - x_p^{(1)}]/\Gamma$ indicates that the two plates tend to stay in contact. The white region (plates separated) and grey region (plates in contact) are separated by Cr_p and $1 - Cr_p$.

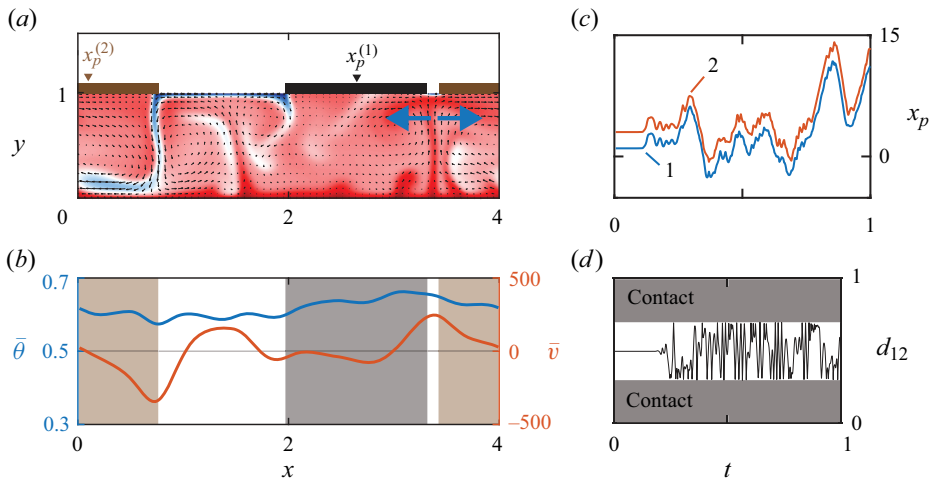


Figure 10. Two large plates ($Cr_p = 0.3$ each) cannot form a stable supercontinent of $Cr = 2Cr_p = 0.6$. (a) The warm upwelling fluid creates a diverging surface flow beneath the plates. This diverging surface flow pulls the two plates apart, rendering the supercontinent formation unstable. (b) Vertically averaged temperature and vertical velocity of the fluid beneath the plates shown in (a). (c) Plate displacements $x_p^{(1)}$ and $x_p^{(2)}$. (d) The normalized plate distance d_{12} stays in the white region where the two plates are separated.

Figure 11 shows how the plate dynamics depends on the combined Cr . In figure 11(a), we define a normalized contact time $\tau = t_c/T$, where t_c is the amount of time that the two plates are in contact, and T is the total simulation time. A sharp decrease of τ is seen near $Cr^* = 1/3$, beyond which a persistent formation of supercontinent is unlikely. This is consistent with our analysis earlier, as a supercontinent with $Cr > Cr^*$ would induce

Covering convection with thermal blankets

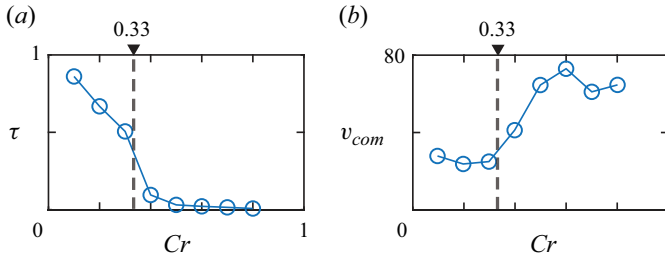


Figure 11. Contact and motion of the plates depend on the covering ratio. (a) The normalized contact time τ decreases sharply when Cr increases above $Cr^* = 1/3$. (b) The plate centre of mass velocity v_{com} increases when $Cr > Cr^*$, indicating that the plates are no longer passive to the flow.

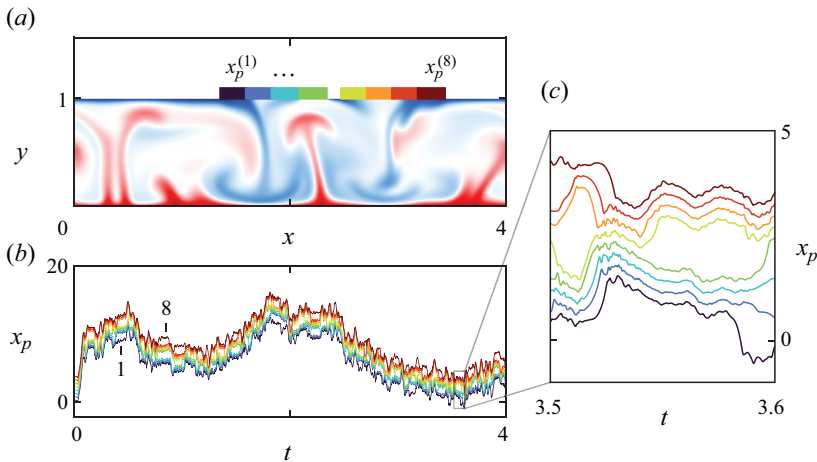


Figure 12. Dynamics of eight plates ($Cr_p = 0.057$, $Cr = 8 Cr_p = 0.457$) floating on top of the convective fluid. (a) A snapshot of eight plates and the convective fluid beneath, where the centre locations of the plates are $(x_p^{(1)}, x_p^{(2)}, \dots, x_p^{(8)})$. (b) Trajectories of $(x_p^{(1)}, x_p^{(2)}, \dots, x_p^{(8)})$; plates can be seen forming supercontinents over time. (c) Zoomed-in view of the trajectories in (b) in the time window $t \in (3.5, 3.6)$.

warm upwelling flows that disintegrate the supercontinent. The centre of mass velocity of plates also picks up when $Cr > Cr^*$ (figure 11b), suggesting that the two large plates are no longer passive but instead translate as we have seen in figure 6(c).

We now see the role of Cr^* in the formation of supercontinents: it is possible to have a stable supercontinent only if its Cr is less than Cr^* .

4.3. Multiple plates

Further increasing the number of plates, the formation of supercontinents exhibits complex and intriguing dynamics. In figure 12 and supplementary movie 5, eight plates with $Cr_p = 0.057$ (total $Cr = 0.457$) are released on top of the convective fluid, where $Ra = 10^6$, $Pr = 7.9$, $\Gamma = 4$, $m = 4d$. The plate maximum interaction force $f_{max} = 10^6$ and interaction range $\delta = \epsilon$ are the same as before.

Figure 12(a) shows a moment when the eight plates form two supercontinents, with each supercontinent covering $4 Cr_p = 0.23$ of the free surface. Each supercontinent thus has a covering ratio less than $Cr^* = 1/3$, and is thereby stable by our earlier argument. Indeed, the stable formation of a supercontinent of four plates can be seen on the plate trajectory

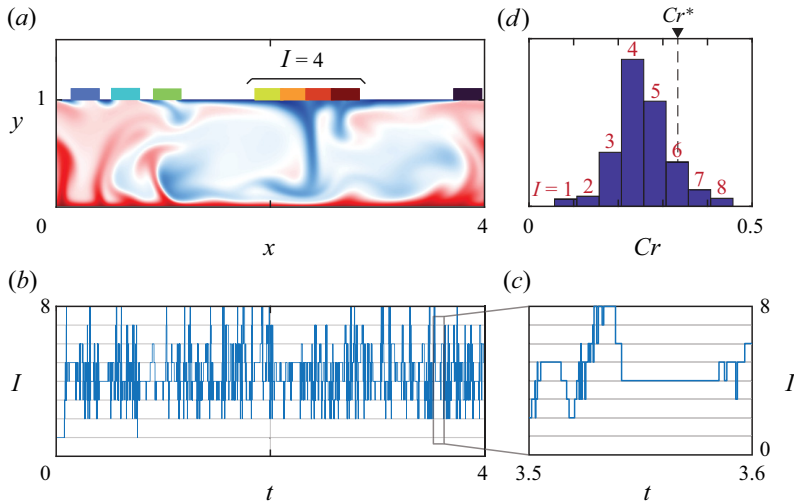


Figure 13. Statistics of the formation number $I(t)$ that is the maximum number of plates in a supercontinent at time t . (a) Schematic of $I = 4$. (b) Time series of $I(t)$ shows the possibility of forming supercontinents with various sizes. (c) Zoomed-in view of $I(t)$ in (b) for $t \in (3.5, 3.6)$. (d) Histogram of $I(t)$ indicates that $I = 4$ is the most common supercontinent formation, while small and large supercontinents are unlikely to form. The histogram is plotted against the size of supercontinent $Cr = ICr_p$, and the formation number I is labelled on top of each bin.

$(x_p^{(1)}, x_p^{(2)}, \dots, x_p^{(8)})$ shown in figure 12(b), whose zoomed-in view for $t \in (3.5, 3.6)$ is shown in figure 12(c). Of course, the formation of a supercontinent with a different number of plates is possible, and our theory predicts that they are stable if the number of plates is $I < Cr^*/Cr_p \approx 6$.

To further analyse the formation of supercontinents, we define the formation number $I(t)$ as the number of plates forming the largest supercontinent at any given time t . A schematic of such a formation number is shown in figure 13(a), where five continents are formed and the largest supercontinent has $I = 4$. The formation number can be tracked over time, and figure 13(b) shows the formation number of the simulation presented in figure 12, with the zoomed-in view of $I(t)$ in the window of figure 12(c) shown in figure 13(c). We note that the formation number can actually take on all integer values between 1 and 8, although many of the formation numbers are transient (such as $I = 1$ and $I = 8$). The most common and persistent formation number that we can see visually in figure 13(c) is $I = 4$, and this is confirmed in the histogram of $I(t)$ shown in figure 13(d).

In figure 13(d), each bin corresponds to the total number of appearances of supercontinents with size I (shown on top of each bin), and the horizontal axis shows the corresponding covering ratio. We indeed see that $I = 4$ plates is the most frequent size of a supercontinent. For small supercontinents, they tend to merge and form a larger but stable supercontinent. For a large supercontinent, the random fluid forcing can trigger a disintegration and break it into many smaller ones. Especially for $I \geq 6$, our theory predicts that such formations are not stable, hence supercontinents with $I \geq 6$ are rarely formed and (once formed) are unstable.

The results shown in figures 12 and 13 are common for simulations with different numbers (N_p) and sizes (Cr_p) of plates. And we identify $ICr_p < Cr^*$ as a clue for predicting the supercontinental size I .

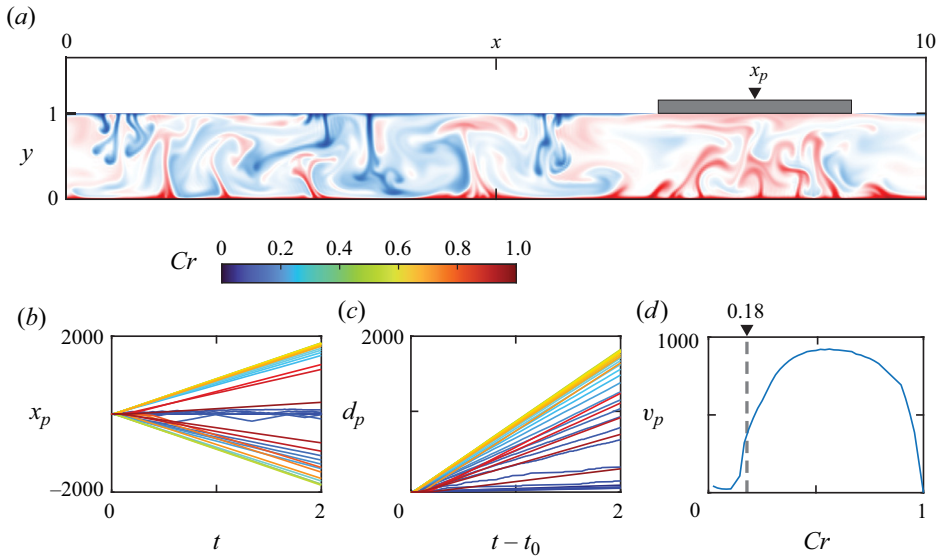


Figure 14. Single-plate dynamics for large aspect ratio convection, where $\Gamma = 10$, $Ra = 10^7$ and $Pr = 7.9$. (a) Typical convective flow field for a plate with covering ratio 0.2. (b) Trajectories of the plate location x_p , where small plates move passively but large plates translate unidirectionally. (c) Total travel of the plate d_p shows the same trend as in (b). (d) Average travel speed v_p has a sharp increase near $Cr^* = 0.18$, which is the critical covering ratio for $\Gamma = 10$. Additional simulations of small and large plates can be found in supplementary movies 6 and 7.

4.4. Convection with increased Ra and Γ

In this subsection, we show examples with Rayleigh number $Ra = 10^7$, Prandtl number $Pr = 7.9$, and domain aspect ratio $\Gamma = 10$. Although these parameters deviate from previous laboratory and numerical investigations, they are actually closer to the conditions of mantle convection (Whitehead & Behn 2015).

We first investigate the single-plate dynamics in figure 14, where the typical flow and temperature fields are shown in figure 14(a). Much like the observations made in figures 4–6, figures 14(b) and 14(c) show that small plates have little motion and are passive to the flow structure, while large plates translate unidirectionally. Typical simulations for a small plate with $Cr = 0.125$ and a large plate with $Cr = 0.417$ are included as supplementary movies 6 and 7.

In figure 14(d), the plate velocity v_p is significantly higher than in figure 6(c), where $Ra = 10^6$. This is consistent with the model introduced in Huang (2024), which suggests that the equilibrium plate velocity is proportional to the surface flow rate. From the classic scaling $Re \sim Ra^{0.5}$ of Rayleigh–Bénard convection (Huang & Zhang 2022), we infer that the flow rate for $Ra = 10^7$ should be $\sqrt{10}$ times bigger than that of $Ra = 10^6$. The plate velocity in figure 14(d) is indeed approximately 3–5 times higher than the velocity shown in figure 6(c), which is consistent with our estimation. Therefore, the Ra value of the convecting fluid directly affects the plate speed, and we note that higher Ra also introduces finer flow structures shown in figure 14(a) that can potentially modify the strength and distribution of the stochastic fluid forcing.

Another difference between figures 14(d) and 6(c) is the critical covering ratio Cr^* differentiating the passive and translating states of the plate. In figure 14(d), a significant

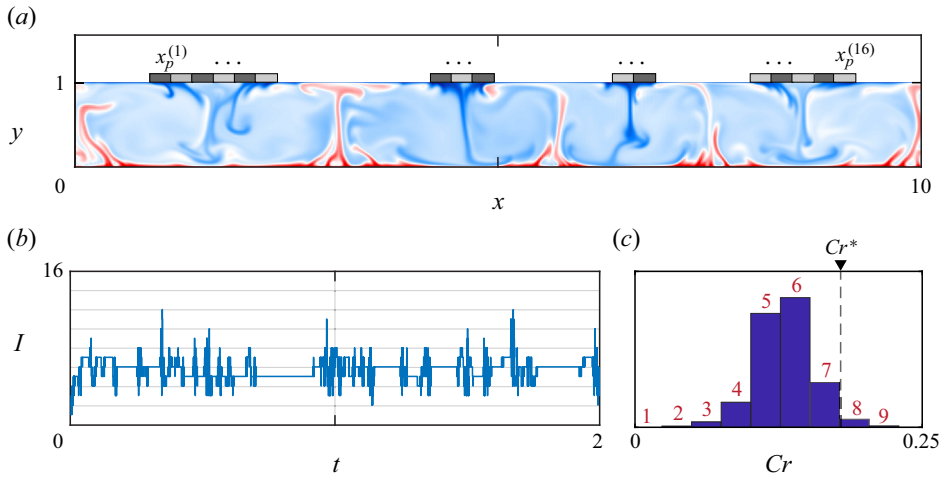


Figure 15. Multiple plate dynamics for large aspect ratio convection. There are 16 plates with individual covering ratio $Cr_p = 0.0234$. The convection parameters are $\Gamma = 10$, $Ra = 10^7$ and $Pr = 7.9$. (a) Typical convective flow field below the 16 moving plates; small groups of supercontinents can be seen. (b) Formation number $I(t)$ indicating the size of the largest supercontinent at time t . (c) Histogram of the formation number I , showing that $I = 6$ is the most probable formation of supercontinents, and that the formation of supercontinents with covering ratio above critical is rare. Supplementary movie 8 is associated with this simulation.

increase in v_p appears at approximately $Cr^* = 0.18$, which is smaller than $Cr^* = 0.33$ in figure 6(c), where $\Gamma = 4$. In Huang (2024), the critical covering ratio Cr^* is shown to depend on the aspect ratio as $Cr^*(\Gamma) \sim \Gamma^{-2/3}$. So $Cr^*(10) = Cr^*(4) (10/4)^{-2/3} = 0.18$, consistent with the data shown in figure 14(d). Therefore the critical covering ratio Cr^* decreases with increasing Γ , while the associated plate length $d^* = \Gamma Cr^* \sim \Gamma^{1/3}$ increases weakly with Γ .

We finally look at the formation of supercontinents at high Ra and Γ . Figure 15(a) shows a typical moment of supercontinent formation, where continents formed by 6, 3, 2 and 5 plates can be seen. In figure 15, each plate has a covering ratio $Cr_p = 0.0234$, and supplementary movie 8 shows this simulation.

In figure 15(a), we can see that the largest supercontinent formation still sits on a converging centre of surface flow, thus making such a formation stable. As we have done in the previous subsection, we define the formation number I as the size of the largest supercontinent at a given time, so $I = 6$ for the moment shown in figure 15(a). The time series of this formation number is shown in figure 15(b), where a formation size of approximately 5–6 plates is common, but both the large and small formations are rare. The histogram of $I(t)$ in figure 15(c) also shows that the most probable supercontinent formation has $I = 6$, whose total covering ratio $Cr = I Cr_p = 0.14$ is smaller than the critical covering ratio $Cr^* = 0.18$ that we identified earlier. In fact, figure 15(c) shows that the formation of $I = 7$ is not rare either, and this is consistent with our estimation that the largest stable supercontinent can have a size up to $Cr^*/Cr_p = 7.7$.

In the discussions above, we see once again that the condition $I Cr_p < Cr^*$ can serve as an indicator of stable supercontinent formation.

5. Discussion

Through our numerical investigations, we clearly see the covering ratio as the main factor affecting the thermal blanket effect, which determines the plate dynamics. This is especially apparent during the formation of supercontinents – the continent covering ratio cannot exceed Cr^* , as the strong thermal blanket effect will induce a diverging surface flow that pulls the formed supercontinent apart.

As our current study is inspired by laboratory experiments, we certainly look forward to future experimental investigations of the interaction between multiple plates. Besides the geometry presented in [figures 1 and 2](#), the broader investigation of fluid–structure interactions in thermal convection also includes adding fixed obstacles to the convective domain (Bao *et al.* 2015; Li, Chen & Xi 2024), modifying the convective boundary conditions (Zhang *et al.* 2020; Huang & Zhang 2022), and allowing for moving boundaries that are driven by the fluid forcing (Mercier *et al.* 2014; Wang & Zhang 2023) or phase change (Huang, Shelley & Stein 2021; Huang & Moore 2022; Weady *et al.* 2022). Many of these works are certainly geophysically inspired, addressing long-standing mysteries such as the super rotation of Earth's inner core (Wang & Zhang 2023; Yang & Song 2023).

In order to simulate the geophysical plate tectonics more closely, there are several future directions to improve our model. The first is to investigate the plate tectonics in a three-dimensional geometry, including the mantle-like spherical shell and the rectangular cuboidal fluid domain that is periodic in two horizontal directions. Although our current numerical scheme is two-dimensional, it can be extended easily to a higher dimension: for the spherical shell geometry, we can adopt a Fourier–Chebyshev–Chebyshev method that solves the heat and flow equations in spherical coordinates; for the periodic cuboidal domain, another periodic horizontal direction can be accommodated by the Fourier method. We are currently working on the three-dimensional study of plate tectonics, and we note that pioneer works including Lowman & Gable (1999), Mao *et al.* (2019) and Mao (2021) have investigated the fluid–structure interactions and plate interactions in these settings. They also used the geophysical parameters of the mantle, most notably Prandtl number approximately 10^{23} (Meyers *et al.* 1987). One modification to accommodate this high Prandtl number is to take an asymptotic limit $Pr \rightarrow \infty$, so the Navier–Stokes equation (2.1) becomes a time-independent Stokes equation (Mao 2021). This Stokes equation can be handled easily by the numerical method in § 3; however, we choose to keep the fluid inertia so our results can be validated by future laboratory experiments, where the working fluid (water) has $Pr = 1–10$.

In our study, we have also set the bottom boundary condition to be no-slip, which is consistent with the experiments. However, this is different from past geophysical models of the mantle, where the bottom boundary is typically assumed to be stress-free at the liquid–liquid interface between the mantle and the outer core of Earth. In the future, we plan to adopt the stress-free bottom condition as it is more consistent with the geophysical settings. Descending deeper into Earth, the outer core meets the solid inner core that is known to rotate. Together with the recent discovery that this rotation is not unidirectional (Yang & Song 2023), a fluid–structure interaction problem thus arises: Does the outer-core convection provide enough shear stress to rotate the inner core? This possibility has inspired some recent experimental developments (Wang & Zhang 2023), and we wish to further engage with this fluid–structure interaction problem in the future.

The interaction between continental plates is also more complicated in geophysical plate tectonics, as the converging continental plates deform the contact region and form the tallest mountains of Earth. It is still an ongoing quest to understand the consequences of converging and diverging continents, with many recent works focusing on the deforming

contact region and addressing its influence on the mantle flow beneath (Rozel *et al.* 2017; Whitehead 2023). Inspired by the geophysics, one modification to our current model could be changing the way in which neighbouring plates interact. This can be achieved through changing the coefficient of restitution to 0 during each collision, which better captures the collision between continental plates during a long time scale. Adding an attractive force between plates can also reveal interesting dynamics, as the diverging surface flow has to be strong enough to pull the plates apart. Thus a larger formation of translating supercontinent may stay stable in this case, and the contact state of plates would also become more persistent. Looking forward, more sophisticated models are required to capture different plate interactions and resulting plate dynamics, and they may reveal new insights into the physics and dynamics of the formation of supercontinents.

To conclude, we consider a toy model to predict the size of the largest continental plate. The aspect ratio of Earth’s mantle is approximately $\Gamma_E = 10$, so the critical covering ratio there is $Cr_E^* \approx 0.18$, as we have estimated in § 4.4. This gives an estimated dimension of the largest stable continental plate of Earth, $L \approx 2\pi R_E Cr_E^*$, where $R_E = 6400$ km is the radius of Earth. So the plate area is $L^2 \approx 6 \times 10^7$ km², slightly underestimating the largest continental plate, the North American Plate, whose area is 7.59×10^7 km².

Supplementary movies. Supplementary movies are available at <https://doi.org/10.1017/jfm.2024.1231>.

Acknowledgements. I thank J.-Q. Zhong, J. Chu and J. Zhang for useful discussions.

Funding. I acknowledge support from the National Natural Science Foundation of China (12272237, 92252204).

Declaration of interests. The author reports no conflict of interest.

Author ORCID.

 Jinzi Mac Huang <https://orcid.org/0000-0003-4277-5851>.

Appendix A. Helmholtz solver for Dirichlet problems

We outline the numerical solver for the following Helmholtz problem:

$$\nabla^2 u - \sigma u = h(x, y), \tag{A1}$$

$$u(x, 0) = g_0(x), \tag{A2}$$

$$u(x, 1) = g_1(x). \tag{A3}$$

As the domain is periodic in $x \in (0, \Gamma]$, we can discretize x as L equally spaced nodes so $x_l = l \Delta x$, where $\Delta x = \Gamma/L$, and $l = 1, 2, \dots, L$. We further require L to be odd. We can now approximate the solution $u(x, y)$ as a truncated Fourier series in x :

$$u(x_l, y) = \sum_{k=-(L-1)/2}^{(L-1)/2} \hat{u}_k(y) \exp(2\pi i k l / L), \tag{A4}$$

where i is the imaginary unit. The Fourier coefficients \hat{u}_k then satisfy the ODE

$$\frac{d^2 \hat{u}_k}{dy^2} - \sigma_k \hat{u}_k = \hat{h}_k(y), \tag{A5}$$

$$\hat{u}_k(0) = \hat{g}_{0,k}, \tag{A6}$$

$$\hat{u}_k(1) = \hat{g}_{1,k}, \tag{A7}$$

where

$$\sigma_k = \frac{4\pi^2 k^2}{\Gamma^2} + \sigma, \tag{A8}$$

$$\hat{h}_k(y) = \frac{1}{L} \sum_{l=1}^L h(x_l, y) \exp(-2\pi ikl/L), \tag{A9}$$

$$\hat{g}_{0,k} = \frac{1}{L} \sum_{l=1}^L g_0(x_l) \exp(-2\pi ikl/L), \tag{A10}$$

$$\hat{g}_{1,k} = \frac{1}{L} \sum_{l=1}^L g_1(x_l) \exp(-2\pi ikl/L). \tag{A11}$$

The computation of (A9)–(A11) can be done efficiently with the help of the fast Fourier transformation algorithm.

Now all that is left is a set of ODEs (A5)–(A7), which can be solved with methods such as finite differences. We instead use the Chebyshev method, and discretize $y \in [0, 1]$ to $M + 1$ Chebyshev nodes, so $y_m = [1 + \cos(m\pi/M)]/2$ with $m = 0, 1, 2, \dots, M$. An advantage of using the Chebyshev method is that the unevenly distributed Chebyshev nodes have a higher resolution near the boundaries $y = 0$ and $y = 1$, therefore resolving the boundary layer structures. The differentiation operator d/dy can be approximated by a discrete operator \mathbf{D} (Trefethen 2000; Peyret 2002) whose elements are

$$D_{j,k} = 2 \frac{c_j}{c_k} \frac{(-1)^{j+k}}{\cos(j\pi/M) - \cos(k\pi/M)}, \quad 0 \leq j, k \leq M, j \neq k, \tag{A12}$$

$$D_{j,j} = -\frac{\cos(j\pi/M)}{1 - \cos^2(j\pi/M)}, \quad 1 \leq j \leq M - 1, \tag{A13}$$

$$D_{0,0} = -D_{M,M} = \frac{2M^2 + 1}{3}. \tag{A14}$$

Here, $c_0 = c_M = 2$, and $c_j = 1$ for $1 \leq j \leq M - 1$.

The discrete operation on the left-hand side of (A5) can therefore be written as

$$\mathbf{A} = \mathbf{D}^2 - \sigma_k \mathbf{I}, \tag{A15}$$

where \mathbf{I} is an $M + 1$ by $M + 1$ identity matrix.

Noticing that the Chebyshev nodes are $\mathbf{y} = [1, y_1, y_2, \dots, y_{M-1}, 0]^T$, we can write the discrete solution to (A5)–(A7) at these locations as a column vector

$$\mathbf{U} = [\hat{g}_{1,k}, \hat{u}_k(y_1), \hat{u}_k(y_2), \dots, \hat{u}_k(y_{M-1}), \hat{g}_{0,k}]^T = [\hat{g}_{1,k}, \tilde{\mathbf{U}}, \hat{g}_{0,k}]^T. \tag{A16}$$

The interior solution $\tilde{\mathbf{U}}$ therefore satisfies

$$\tilde{\mathbf{A}}\tilde{\mathbf{U}} = \tilde{\mathbf{H}}, \tag{A17}$$

where the $(M - 1) \times (M - 1)$ matrix $\tilde{\mathbf{A}}$ is the interior of \mathbf{A} (by removing its first and last rows and columns), and

$$\tilde{\mathbf{H}} = \begin{bmatrix} \hat{h}_k(y_1) - \hat{g}_{1,k}A_{1,1} - \hat{g}_{0,k}A_{1,M} \\ \hat{h}_k(y_2) - \hat{g}_{1,k}A_{2,1} - \hat{g}_{0,k}A_{2,M} \\ \vdots \\ \hat{h}_k(y_{M-1}) - \hat{g}_{1,k}A_{M-1,1} - \hat{g}_{0,k}A_{M-1,M} \end{bmatrix}. \tag{A18}$$

Equation (A17) is invertible, and the operator $\tilde{\mathbf{A}}$ does not change during time stepping, while the boundary information g and forcing h are contained in $\tilde{\mathbf{H}}$. This allows us to compute the LU decomposition of $\tilde{\mathbf{A}}$ at the beginning so $\tilde{\mathbf{A}}\tilde{\mathbf{U}} = \tilde{\mathbf{H}}$ can be inverted efficiently through backward and forward substitutions during time stepping. With $\tilde{\mathbf{U}}$ and \mathbf{U} solved, the Fourier coefficients \hat{u}_k can then be inserted into (A4), and the solution $u(x, y)$ is therefore obtained.

Appendix B. Helmholtz solver for Robin boundary conditions

Next, we consider the Helmholtz solver for equations such as (3.2), where inhomogeneous Robin boundary conditions such as (2.11) are applied. In a general form, consider

$$\nabla^2 u - \sigma u = h, \tag{B1}$$

$$a_0(x) u(x, 0) + b_0(x) u_y(x, 0) = g_0(x), \tag{B2}$$

$$a_1(x) u(x, 1) + b_1(x) u_y(x, 1) = g_1(x). \tag{B3}$$

The idea for solving these equations is to use the influence matrix method (Peyret 2002): a PDE with inhomogeneous Robin boundary conditions can be converted into a series of PDEs with homogeneous Dirichlet boundary conditions, which can be solved by the method detailed in Appendix A.

We first separate the solution into several subproblems, so

$$u(x, y) = \tilde{u}(x, y) + \sum_{l=1}^{2L} \xi_l \bar{u}_l(x, y), \tag{B4}$$

where ξ_l are unknown coefficients to be determined later, and

$$\nabla^2 \tilde{u} - \sigma \tilde{u} = h, \tag{B5}$$

$$\tilde{u}(x, 0) = \tilde{u}(x, 1) = 0, \tag{B6}$$

$$\nabla^2 \bar{u}_l - \sigma \bar{u}_l = 0, \tag{B7}$$

$$\bar{u}_l|_{\eta_m} = \delta_{lm} \quad \text{for all } \eta_m \in \partial\Omega. \tag{B8}$$

Here, η_m represents the m th node on the boundary, so there are $2L$ of them, and δ_{lm} is the Kronecker delta function. Now, the boundary conditions (B2) and (B3) indicate

$$\left[a_i(x) \left(\sum_{l=1}^{2L} \xi_l \bar{u}_l \right) + b_i(x) \left(\frac{\partial \tilde{u}}{\partial y} + \sum_{l=1}^{2L} \xi_l \frac{\partial \bar{u}_l}{\partial y} \right) - g_i(x) \right] \Big|_{\eta_m} = 0 \quad \text{for } \eta_m \in \partial\Omega. \tag{B9}$$

Here, $i \in \{0, 1\}$ indicates the bottom or top boundary. As (B9) holds on all the boundary nodes η_m , it provides $2L$ equations for $2L$ unknowns ξ_l , and such a linear system is

invertible. With all ξ_l solved, the solution of (B1)–(B3) can be recovered as $u = \tilde{u} + \sum_{l=1}^{2L} \xi_l \bar{u}_l$.

In fact, ξ_m is exactly the Dirichlet data for u at boundary node η_m , therefore the solution of (B1)–(B3) is the same as the solution of

$$\nabla^2 u - \sigma u = h, \tag{B10}$$

$$u|_{\eta_m} = \xi_m \quad \text{for } \eta_m \in \partial\Omega. \tag{B11}$$

This method can directly solve the heat equation (3.2) with boundary conditions in (2.8) and (2.12), by assigning $a_0 = 1$, $b_0 = 0$, $g_0 = 1$ at the bottom, and $a_1 = 1 - a$, $b_1 = a$, $g_1 = 0$ at the top. Usually, the solutions of (B7) and (B8) are obtained and saved at the beginning. At each time step, (B5) and (B6) are solved, and the location of moving plates will determine $a_i(x)$, $b_i(x)$ and $g_i(x)$, so (B9) can be inverted to provide ξ_m , which can be used as boundary data in (B10) and (B11), and the solution θ_n can therefore be determined.

Appendix C. Flow solver with Robin boundary conditions

At each time step, the following flow problem must be solved:

$$\nabla^2 \omega - \sigma \omega = f, \tag{C1}$$

$$-\nabla^2 \psi = \omega, \tag{C2}$$

$$\psi = \psi_y = 0 \quad \text{at } y = 0, \tag{C3}$$

$$\psi = 0, a\psi_y + (1 - a)\psi_{yy} = g \quad \text{at } y = 1. \tag{C4}$$

Here, we have dropped all the subscripts. We can also solve these equations with the influence matrix method. Now we want to convert the Neumann boundary condition in (C3) and Robin boundary condition in (C4) to a Dirichlet boundary condition for vorticity ω . We decompose ω and ψ as

$$\omega(x, y) = \tilde{\omega}(x, y) + \sum_{l=1}^{2L} \xi_l \bar{\omega}_l(x, y), \tag{C5}$$

$$\psi(x, y) = \tilde{\psi}(x, y) + \sum_{l=1}^{2L} \xi_l \bar{\psi}_l(x, y). \tag{C6}$$

The associated subproblems are

$$\nabla^2 \tilde{\omega} - \sigma \tilde{\omega} = f, \quad -\nabla^2 \tilde{\psi} = \tilde{\omega}, \tag{C7a,b}$$

$$\tilde{\omega}(x, 0) = \tilde{\omega}(x, 1) = \tilde{\psi}(x, 0) = \tilde{\psi}(x, 1) = 0, \tag{C8}$$

$$\nabla^2 \bar{\omega}_l - \sigma \bar{\omega}_l = 0, \quad -\nabla^2 \bar{\psi}_l = \bar{\omega}_l, \tag{C9}$$

$$\bar{\psi}_l(x, 1) = 0, \bar{\omega}_l|_{\eta_m} = \delta_{lm} \quad \text{for all } \eta_m \in \partial\Omega. \tag{C10}$$

The Neumann boundary condition in (C3) and the Robin boundary condition in (C4) can now be enforced as

$$\left(\frac{\partial \tilde{\psi}}{\partial y} + \sum_{l=1}^{2L} \xi_l \frac{\partial \bar{\psi}_l}{\partial y} \right) \Big|_{\eta_m} = 0 \quad \text{for } \eta_m \in \partial\Omega_0, \tag{C11}$$

$$\left[a \left(\frac{\partial \tilde{\psi}}{\partial y} + \sum_{l=1}^{2L} \xi_l \frac{\partial \tilde{\psi}_l}{\partial y} \right) + (1-a) \left(\frac{\partial^2 \tilde{\psi}}{\partial y^2} + \sum_{l=1}^{2L} \xi_l \frac{\partial^2 \tilde{\psi}_l}{\partial y^2} \right) - g \right] \Big|_{\eta_m} = 0 \quad \text{for } \eta_m \in \partial\Omega_1. \tag{C12}$$

Equations (C11) and (C12) are again $2L$ equations for $2L$ unknowns ξ_l , and the linear system is invertible. Equations (C5) and (C6) can then be summed, and the solutions are obtained. In fact, ξ_l is exactly the boundary data for ω at boundary node η_l , so we can instead solve

$$\nabla^2 \omega - \sigma \omega = f, \tag{C13}$$

$$-\nabla^2 \psi = \omega, \tag{C14}$$

$$\psi|_{\eta_m} = 0, \omega|_{\eta_m} = \xi_m \quad \text{for } \eta_m \in \partial\Omega. \tag{C15}$$

Appendix D. Summary of numerical methods

There are two stages during our numerical simulation, and below we list some of the key steps during each stage.

Pre-processing stage steps.

- (i) The inverse $\tilde{\mathbf{A}}^{-1}$ (or the LU decomposition of $\tilde{\mathbf{A}}$) in (A17) is prepared for operators in (3.1)–(3.3), by taking $\sigma = 0, \sigma_1, \sigma_2$ in (A15).
- (ii) Subproblems (B7)–(B8) and (C9)–(C10) are solved, and the solutions $\bar{\theta}_l, \bar{\omega}_l$ and $\bar{\psi}_l$ for $l = 1, 2, \dots, 2L$ are saved.

Steps at the n th step of the time stepping stage.

- (i) The fluid and interaction forces on each plate are computed according to (3.15)–(3.17).
- (ii) The location and velocity of each plate are evolved by (3.7) and (3.8), and the indicator function \hat{a} is prepared by (3.14a,b).
- (iii) The forcing term h_n in (3.2) is prepared according to (3.6), and $\tilde{\theta}_l$ is solved from (B5) and (B6).
- (iv) Equation (B9) is inverted so the Dirichlet boundary data for θ_n are known; (B10) and (B11) are then solved for θ_n .
- (v) The temperature θ_n is used to prepare f_n according to (3.5), so $\tilde{\omega}_l, \tilde{\psi}_l$ can be solved from (C7a,b) and (C8).
- (vi) Equations (C11) and (C12) are inverted so the Dirichlet data for ω_n are known; (C14) and (C15) are finally solved to provide ω_n and ψ_n .

For simulations with $\Gamma = 4$, we use $L = 256$ Fourier nodes and $M + 1 = 65$ Chebyshev nodes. For simulations with higher aspect ratio $\Gamma = 10$, $L = 512$ Fourier nodes and $M + 1 = 65$ Chebyshev nodes are used instead. During time stepping, we typically set $\Delta t = \tau_0 = 5 \times 10^{-4} Ra^{-1/2}$ considering that the flow speed is $|\mathbf{u}| \sim \sqrt{Ra}$.

These parameters are tested to yield spatially and temporally resolved results. In table 1, time-averaged values of Nu, Re and v_p (plate speed) are measured at the dynamical equilibrium state of convection with $Ra = 10^7, Pr = 7.9$ and $\Gamma = 10$, where a floating plate with $Cr = 1/2$ is free to move on top. The convergence of these values shows that

	L	M	Δt	Nu	Re	v_p
	256	40	$2\tau_0$	13.4	492	963
	256	40	τ_0	13.3	492	964
	256	40	$0.5\tau_0$	13.4	493	965
	512	64	$2\tau_0$	12.7	489	928
*	512	64	τ_0	12.8	491	925
	512	64	$0.5\tau_0$	12.8	493	920
	1024	128	$2\tau_0$	12.8	493	918
	1024	128	τ_0	12.8	490	915
	1024	128	$0.5\tau_0$	12.8	490	915

Table 1. Time-averaged dynamical quantities at different spatial and temporal resolutions for plate tectonics with $Ra = 10^7$, $Pr = 7.9$, $\Gamma = 10$ and $Cr = 1/2$. Here, L is the number of Fourier modes, $M + 1$ is the number of Chebyshev nodes, and Δt is the time step size. The asterisked parameters are used in the direct numerical simulations of figures 14 and 15, where $\Delta t = \tau_0 = 5 \times 10^{-4} Ra^{-1/2}$.

our choice of spatial and temporal resolution is sufficient to resolve the dynamics of the flow and the plate.

REFERENCES

- AHLERS, G., GROSSMANN, S. & LOHSE, D. 2009 Heat transfer and large scale dynamics in turbulent Rayleigh–Bénard convection. *Rev. Mod. Phys.* **81** (2), 503.
- ARAUJO, F.F., GROSSMANN, S. & LOHSE, D. 2005 Wind reversals in turbulent Rayleigh–Bénard convection. *Phys. Rev. Lett.* **95** (8), 084502.
- BAO, Y., CHEN, J., LIU, B.-F., SHE, Z.-S., ZHANG, J. & ZHOU, Q. 2015 Enhanced heat transport in partitioned thermal convection. *J. Fluid Mech.* **784**, R5.
- BROWN, E. & AHLERS, G. 2007 Large-scale circulation model for turbulent Rayleigh–Bénard convection. *Phys. Rev. Lett.* **98** (13), 134501.
- BURKE, K. 2011 Plate tectonics, the Wilson cycle, and mantle plumes: geodynamics from the top. *Annu. Rev. Earth Planet. Sci.* **39**, 1–29.
- CHERNIH, A., SLOAN, I.H. & WOMERSLEY, R.S. 2014 Wendland functions with increasing smoothness converge to a Gaussian. *Adv. Comput. Maths* **40** (1), 185–200.
- ELDER, J. 1967 Convective self-propulsion of continents. *Nature* **214** (5089), 657–660.
- GURNIS, M. 1988 Large-scale mantle convection and the aggregation and dispersal of supercontinents. *Nature* **332** (6166), 695–699.
- HOU, T.Y. & LI, R. 2007 Computing nearly singular solutions using pseudo-spectral methods. *J. Comput. Phys.* **226** (1), 379–397.
- HOWARD, L.N., MALKUS, W.V.R. & WHITEHEAD, J.A. 1970 Self-convection of floating heat sources: a model for continental drift. *Geophys. Astrophys. Fluid Dyn.* **1** (1–2), 123–142.
- HUANG, J.M. 2024 Covering convection with a thermal blanket: numerical simulation and stochastic modelling. *J. Fluid Mech.* **980**, A47.
- HUANG, J.M. & MOORE, N.J. 2022 Morphological attractors in natural convective dissolution. *Phys. Rev. Lett.* **128** (2), 024501.
- HUANG, J.M., SHELLEY, M.J. & STEIN, D.B. 2021 A stable and accurate scheme for solving the Stefan problem coupled with natural convection using the immersed boundary smooth extension method. *J. Comput. Phys.* **432**, 110162.
- HUANG, J.M. & ZHANG, J. 2022 Rayleigh–Bénard thermal convection perturbed by a horizontal heat flux. *J. Fluid Mech.* **954**, R2.
- HUANG, J.M., ZHONG, J.-Q., ZHANG, J. & MERTZ, L. 2018 Stochastic dynamics of fluid–structure interaction in turbulent thermal convection. *J. Fluid Mech.* **854**, R5.
- KIOUS, W.J. & TILLING, R.I. 1996 *This Dynamic Earth: The Story of Plate Tectonics*. DIANE Publishing.
- LI, Y.-Z., CHEN, X. & XI, H.-D. 2024 Enhanced heat transfer and reduced flow reversals in turbulent thermal convection with an obstructed centre. *J. Fluid Mech.* **981**, A16.
- LOWENSTEIN, J.H. 2024 Near-critical behavior of the Zhong–Zhang model. *Phys. Rev. E* **109**, 025102.

- LOWMAN, J.P. & GABLE, C.W. 1999 Thermal evolution of the mantle following continental aggregation in 3D convection models. *Geophys. Res. Lett.* **26** (17), 2649–2652.
- LOWMAN, J.P. & JARVIS, G.T. 1993 Mantle convection flow reversals due to continental collisions. *Geophys. Res. Lett.* **20** (19), 2087–2090.
- LOWMAN, J.P. & JARVIS, G.T. 1995 Mantle convection models of continental collision and breakup incorporating finite thickness plates. *Phys. Earth Planet. Inter.* **88** (1), 53–68.
- LOWMAN, J.P. & JARVIS, G.T. 1999 Effects of mantle heat source distribution on supercontinent stability. *J. Geophys. Res.: Solid Earth* **104** (B6), 12733–12746.
- LOWMAN, J.P., KING, S.D. & GABLE, C.W. 2001 The influence of tectonic plates on mantle convection patterns, temperature and heat flow. *Geophys. J. Intl* **146** (3), 619–636.
- MAO, Y. 2021 An insulating plate drifting over a thermally convecting fluid: the effect of plate size on plate motion, coupling modes and flow structure. *J. Fluid Mech.* **916**, A18.
- MAO, Y., ZHONG, J.-Q. & ZHANG, J. 2019 The dynamics of an insulating plate over a thermally convecting fluid and its implication for continent movement over convective mantle. *J. Fluid Mech.* **868**, 286–315.
- MERCIER, M.J., ARDEKANI, A.M., ALLSHOUSE, M.R., DOYLE, B. & PEACOCK, T. 2014 Self-propulsion of immersed objects via natural bioconvection. *Phys. Rev. Lett.* **112** (20), 204501.
- MEYERS, R.A. 1987 *Encyclopedia of Physical Science and Technology*. Academic.
- MOORE, N.J. & HUANG, J.M. 2024 Large-scale circulation reversals explained by pendulum correspondence. *J. Fluid Mech.* **993**, A3.
- PEYRET, R. 2002 *Spectral Methods for Incompressible Viscous Flow*. Springer.
- PLUMMER, C.C., CARLSON, D.H. & HAMMERSLEY, L. 2015 *Physical Geology*. McGraw-Hill.
- ROZEL, A.B., GOLABEK, G.J., JAIN, C., TACKLEY, P.J. & GERYA, T. 2017 Continental crust formation on early Earth controlled by intrusive magmatism. *Nature* **545** (7654), 332–335.
- TREFETHEN, L.N. 2000 *Spectral Methods in MATLAB*. SIAM.
- TURCOTTE, D.L. & SCHUBERT, G. 2002 *Geodynamics*. Cambridge University Press.
- WANG, K. & ZHANG, J. 2023 Persistent corotation of the large-scale flow of thermal convection and an immersed free body. *Proc. Natl Acad. Sci. USA* **120** (21), e2217705120.
- WEADY, S., TONG, J., ZIDOVSKA, A. & RISTROPH, L. 2022 Anomalous convective flows carve pinnacles and scallops in melting ice. *Phys. Rev. Lett.* **128**, 044502.
- WHITEHEAD, J.A. 1972 Moving heaters as a model of continental drift. *Phys. Earth Planet. Inter.* **5**, 199–212.
- WHITEHEAD, J.A. 2023 Convection cells with accumulating crust: models of continent and mantle evolution. *J. Geophys. Res.: Solid Earth* **128** (4), e2022JB025643.
- WHITEHEAD, J.A. & BEHN, M.D. 2015 The continental drift convection cell. *Geophys. Res. Lett.* **42** (11), 4301–4308.
- YANG, Y. & SONG, X. 2023 Multidecadal variation of the Earth's inner-core rotation. *Nat. Geosci.* **16** (2), 182–187.
- ZHANG, J. & LIBCHABER, A. 2000 Periodic boundary motion in thermal turbulence. *Phys. Rev. Lett.* **84** (19), 4361.
- ZHANG, S., XIA, Z., ZHOU, Q. & CHEN, S. 2020 Controlling flow reversal in two-dimensional Rayleigh–Bénard convection. *J. Fluid Mech.* **891**, R4.
- ZHONG, J.-Q. & ZHANG, J. 2005 Thermal convection with a freely moving top boundary. *Phys. Fluids* **17** (11), 115105.
- ZHONG, J.-Q. & ZHANG, J. 2007a Dynamical states of a mobile heat blanket on a thermally convecting fluid. *Phys. Rev. E* **75** (5), 055301.
- ZHONG, J.-Q. & ZHANG, J. 2007b Modeling the dynamics of a free boundary on turbulent thermal convection. *Phys. Rev. E* **76** (1), 016307.
- ZHONG, S. & GURNIS, M. 1993 Dynamic feedback between a continentlike raft and thermal convection. *J. Geophys. Res.: Solid Earth* **98** (B7), 12219–12232.
- ZHONG, S., ZUBER, M.T., MORESI, L. & GURNIS, M. 2000 Role of temperature-dependent viscosity and surface plates in spherical shell models of mantle convection. *J. Geophys. Res.: Solid Earth* **105** (B5), 11063–11082.